Stability of tungsten-doped δ-Bi_3YO_6

A. Borowska-Centkowska,[1*] M. Leszczynska,[1] W. Wrobel,[1] M. Malys,[1] S. Hull,[2] F. Krok,[1] and I. Abrahams,[3*]

[1]Faculty of Physics, Warsaw University of Technology, ul. Koszykowa 75, 00-662, Warsaw Poland.

[2]ISIS Facility, Rutherford Appleton Laboratory, Chilton, Didcot, Oxon OX11 0QX, United Kingdom

[3]Materials Research Institute, School of Biological and Chemical Sciences, Queen Mary University of London, Mile End Road, London E1 4NS, United Kingdom

* corresponding authors:

I. Abrahams e –mail: i.abrahams@qmul.ac.uk
F. Krok e –mail: centkowska@if.pw.edu.pl

Abstract

The stability of bismuth yttrium oxide doped with tungsten, $Bi_3Y_{1-x}W_xO_{6+3x/2,}$ on annealing in air for up to 1000 h at 650 °C was investigated using a.c. impedance spectroscopy and neutron diffraction. Compositions up to $x = 0.2$ all show some degree of conductivity decay, but only in the case of the $x = 0.10$ composition is this decay relatively small and not associated with a significant structural change. Details of the short range structure of this composition were investigated by reverse Monte Carlo modelling of total neutron scattering data and again reveal no significant changes prior to and post annealing. A preference for <100> oxide ion vacancy pair alignment is found in the structure consistent with models for oxide ion conduction in these systems. Additionally, the total scattering analysis reveals a preferred vacancy association with the W^{6+} cations, which adopt a four coordinate geometry in this system.

Keywords: Bismuth yttrium oxide, fluorite, stability, impedance spectroscopy, total neutron scattering.

1. Introduction

The search for materials capable of use in the construction of intermediate temperature solid oxide fuel cells (IT-SOFCs) is the subject of much current research. Arguably, the key component of such devices is the electrolyte, since the choice of electrolyte determines the selection of the electrodes and hence the operational temperature of the device. Despite concern over their stability at low oxygen partial pressures, it has been demonstrated that bismuth oxide based electrolytes can be successfully incorporated into IT-SOFCs [1,2]. While many bismuth oxide based systems show exceptional oxide ion conductivity at intermediate temperatures (*ca*. 500 to 700 °C), there has been much debate about the thermodynamic stability of these materials. This is particularly relevant for their use in IT-SOFCs, since properties such as thermal expansion must be matched to those of the electrode materials.

The highly conducting δ-phase of bismuth oxide, which exhibits the highest oxide ion conductivity of any known solid, is only stable above *ca*. 730 °C [3]. However, its defect fluorite structure may be preserved to ambient temperature through solid solution formation with other oxides [4-9]. The high conductivity of δ-Bi_2O_3 is attributed to its intrinsic high oxide ion vacancy concentration (0.5 vacancies per metal atom) with respect to the ideal fluorite lattice, highly polarizable cation framework and three-dimensional conduction pathways. Isovalent substitution in Bi_2O_3 leads to δ-phase compounds, with nominally the same oxide ion vacancy concentration as in the parent δ-Bi_2O_3. Amongst the most important of these are the rare-earth substituted systems, which show good conductivity. However, significant decay in conductivity is observed on annealing for extended periods at intermediate temperatures [10-14]. For example, it was reported by Watanabe that annealing of δ-Bi_3YO_6 between 500-650 °C for *ca*. 100 h, invariably leads to complete transformation to a rhombohedral phase [15,16]. In comprehensive studies carried out in the group of Waschman, similar behaviour was reported throughout the rare-earth substituted bismuth oxides [10-12,14], confirming the metastability of these systems. In attempts to overcome this inherent metastability, the use of a second substituent to improve stability was investigated. It was observed that low levels of tungsten doping, resulted in significant improvement in the stabilisation of conductivity in bismuth erbium oxide [17] and bismuth dysprosium oxide [14,18].

We have previously investigated defect structure and electrical behaviour in δ-Bi_3YO_6 [19,20]. Using total neutron scattering and energy minimization methods, we found evidence for oxide ion vacancy ordering, which can be correlated with the thermal variation of conductivity in this system. Further studies using *ab initio* molecular dynamics simulations have shown that Y^{3+} acts as a defect trap in δ-Bi_3YO_6 [21,22]. While supervalent dopants such as Nb^{5+} also act as traps for oxide ions, they maintain high oxide ion dynamics, but the motion is mainly restricted to the

coordination sphere of the dopant cation [23]. Indeed, for supervalent dopants, such as Nb^{5+}, Ta^{5+} and W^{6+} the preferred coordination geometry of the dopant cation is particularly important and can lead to ordering phenomena [24]. Most relevant to the present study is the case of tungsten doping in Bi_2O_3, where for example in $Bi_{14}WO_{24}$ the small W^{6+} cation adopts a tetrahedral coordination in the low temperature ordered fluorite phases [25] and maintains this even in the case of the high temperature δ-phase [26]. We have previously shown in the system $Bi_3Y_{1-x}W_xO_{6+3x/2}$ that single δ-Bi_2O_3 type phases can be obtained in the range $0.00 \leq x \leq 0.20$, with little influence on the values of total conductivity [27].

Here we present a comprehensive study of the electrical and structural stability of the δ-$Bi_3Y_{1-x}W_xO_{6+3x/2}$ phases during prolonged annealing at intermediate temperatures. As well as structural stability on the crystallographic scale, the stability of defect structure on annealing at 650 °C for up to 1000 h is investigated by reverse Monte Carlo modelling of total neutron scattering data. The x = 0.10 composition is shown to exhibit excellent structural stability, with minimal conductivity decay.

2. Experimental

2.1 Preparations

Samples of composition $Bi_3Y_{1-x}W_xO_{6+3x/2}$ ($0.00 \leq x \leq 0.20$) were prepared using appropriate amounts of Bi_2O_3 (Aldrich, 99.9%), WO_3 (Aldrich, 99.99%) and Y_2O_3 (Aldrich, 99.99%). The starting mixtures were ground in ethanol using a planetary ball mill. After drying, the mixtures were heated initially at 750 °C for 24 h and after cooling, samples were reground and heated for a further 24 h at 800 °C. A third 24 h heating step was required at 850 °C for the x = 0.20 composition. In each case, samples were slow cooled in the furnace to room temperature over a period of *ca*. 12 h after the final heating step. Pellets of 10 mm diameter and 2-3 mm thickness were pressed isostatically from synthesised powder at a pressure of 400 MPa and sintered for 10 h at 800 °C, 850 °C or 900 °C for x = 0.00, $0.05 \leq x \leq 0.15$ and 0.20 compositions, respectively.

2.2 Diffraction

Ambient temperature X-ray powder diffraction data were collected on a Philips X'Pert Pro X-ray diffractometer fitted with an X'Celerator detector, using Ni filtered Cu-Kα radiation (λ_1 = 1.54056 Å and λ_2 = 1.54439 Å), in flat plate θ/θ geometry on a spinning sample holder. Data collection was carried out in the range 5-125° 2θ, in steps of 0.033°, with an effective scan time of 50 s per step. Calibration was carried out with an external LaB_6 standard.

Powder neutron diffraction data were collected on fresh and annealed samples of the x = 0.05 and 0.10 compositions on the Polaris diffractometer at the ISIS Facility, Rutherford Appleton Laboratory, UK. Samples were placed in 11 mm diameter vanadium cans and data collected on back-scattering (average angle 146.72°), 90° (average angle 92.5°), intermediate-angle (average angle 52.21°), low-angle (average angle 25.99°) and very low angle (average angle 10.4°) detectors, corresponding to the approximate *d*-spacing ranges 0.05-2.65 Å, 0.1-4.1 Å, 0.3-7.0 Å, 0.4-13.5 Å and 1.0-48 Å, respectively. For standard Rietveld analysis, data collections corresponding to proton beam currents of 200 μA h were made, while for total scattering analysis, data sets of 1000 μA h were acquired. For total scattering data correction, a 400 μA h data set was collected on an empty thin walled vanadium can.

2.3 Structure analysis

Structure refinement was carried out by combined Rietveld whole profile fitting of X-ray and neutron data sets using the program GSAS [28]. For the cubic phase, a fluorite model in space group *Fm*-3*m* was used for all refinements, as previously described [19]. Bi, Y and W were located on the ideal 4*a* site (0,0,0), with oxide ions distributed over three sites; 8*c* at (0.25, 0.25, 0.25); 32*f* at approximately (0.3, 0.3, 0.3) and 48*i* at around (0.5, 0.2, 0.2). A total oxide ion occupancy constraint was applied. For the rhombohedral phase, the model of Zhang *et al*. [29] for $Bi_{0.8}Y_{0.2}O_{1.5}$ was used as a starting model, with an appropriate change in stoichiometry.

Neutron diffraction data for the x = 0.10 composition (an un-annealed sample and one that had been annealed for 1000 h) were used in a total scattering study through reverse Monte Carlo (RMC) fitting [30]. Data were summed and corrected for background scattering and beam attenuation using Gudrun [31]. The total radial distribution function, G(r), was obtained by Fourier transformation of the normalized total scattering structure factors, S(Q), (where Q, the scattering vector = $2\pi/d$). Fitting was carried out against the reciprocal space data, S(Q), the real space data, G(r), and the Bragg profile data using RMCProfile [32]. Starting configurations consisted of $10 \times 10 \times 10$ unit cells based on the ideal fluorite structure, with a random distribution of Bi, Y and W atoms over the sites corresponding to the 4*a* site in the cubic *Fm*-3*m* subcell, and anion vacancies randomly distributed over supercell sites corresponding to the 8*c* crystallographic site in the cubic subcell. In each case, parallel calculations were carried out on 10 different random configurations.

Calculations were performed using bond valence summation (BVS) constraints [33] and an O-O potential constraint to avoid unrealistically short O-O contacts. The BVS parameters were taken from Brese and O'Keeffe [34].

2.4 Electrical measurements

Electrical parameters were determined by a.c. impedance spectroscopy in 20 °C steps in the approximate temperature range 300 to 850 °C, using a Solartron 1255/1286 system, over the frequency range 1 Hz to 5×10^5 Hz. Samples were prepared as rectangular blocks (*ca*. $6 \times 3 \times 3$ mm^3) cut from slow cooled sintered pellets using a diamond saw. Platinum electrodes were sputtered by cathodic discharge on the two smallest faces. For standard measurements, impedance spectra were recorded over two cycles of heating and cooling at stabilised temperatures. Impedance at each frequency was measured repeatedly until consistency (2% tolerance in drift) was achieved or a maximum number of 25 repeats had been reached.

The ionic and electronic components of total conductivity were determined using a modified EMF method. Pellets (*ca*. 17 mm in diameter and 2 mm in thickness with Pt electrodes of *ca*. 10 mm diameter) were measured in the concentration cell $O_2(pO_2 = 1.01 \times 10^5$ Pa): Pt | oxide | Pt : O_2 ($pO_2 = 0.2095 \times 10^5$ Pa) with an external adjustable voltage source, as previously described [35]. Measurements were performed on cooling in the approximate temperature range 800 to 500 °C.

2.5 Prolonged annealing studies

For initial structural stability studies, several sintered sample pellets of each composition were placed on a Pt boat and heated to 650 °C in air and maintained at this temperature for *ca*. 200 h. For extended structural stability studies, sintered powders were heated to 650 °C in air, over a period of *ca*. 3 h and samples left at this temperature for periods up to 1000 h, before slow cooling in air to room temperature at a rate of 1° min^{-1}. In both cases subsequent diffraction measurements were performed as described above.

For conductivity stability measurements, the impedance spectra were first recorded on heating to 850 °C and then on cooling to 300 °C, to ensure agreement with standard measurements [27]. In each case, the sample was then heated to 650 °C and isothermal data collected regularly over a period of up to 1150 h. After this time, impedance measurements were made on cooling down to *ca*. 300 °C and a further standard heating/cooling cycle performed.

3. Results and Discussion

Our previous work on the $Bi_3Y_{1-x}W_xO_{6+3x/2}$ system established that only in the range $0.00 \leq x \leq 0.20$ were single phase compositions obtained [27]. In addition, there was very little change in total conductivity from ambient temperature up to *ca*. 850 °C between compositions. Our stability studies were therefore confined to the compositions $x = 0.00$, 0.05, 0.10, 0.15 and 0.20.

Fig. 1 shows X-ray powder diffraction patterns of all compositions studied after annealing at 650 °C for 200 h. The pattern for the $x = 0.00$ composition exhibits additional peaks corresponding

to the rhombohedral phase as reported previously [15,16]. The pattern for the $x = 0.05$ composition shows very little change after 200 h, although close inspection reveals very weak peaks corresponding to the rhombohedral phase. The $x = 0.10$ composition shows no visible change in the diffraction pattern after 200 h. The diffraction patterns for the $x = 0.15$ and $x = 0.20$ compositions both show additional peaks after 200 h corresponding to an unidentified secondary phase.

Fig. 2 shows Arrhenius plots of total conductivity for the $x = 0.00$ composition, including data for isothermal annealing at 650 °C for *ca*. 1100 h. The initial heating and cooling plots show two linear regions, one at low temperatures with an activation energy of 1.178(2) eV and one at high temperatures with a lower activation energy of 0.73(1) eV, with a transition between the two regions at around 600 °C. The values compare favourably with those previously reported [20]. On annealing at 650 °C, the conductivity is seen to drop significantly and on cooling after *ca*. 1100 h, Arrhenius behaviour is observed with an activation energy of 1.10 eV. On subsequent heating, the conductivity follows that of the post anneal cooling up to around 450 °C, where the plots begin to diverge and at around 700 °C the conductivity sharply recovers to that observed prior to the annealing experiment. Subsequent cooling follows the pre-annealing behaviour. Similar behaviour is observed in the parallel experiments for the $x = 0.05$, 0.15 and 0.20 compositions (Supporting Information Figs. S1 to S3). In the case of the $x = 0.10$ composition (Fig. 3), the conductivity decay at 650 °C after 1000 h is much reduced in comparison to that observed in the other studied compositions. Table 1 summarises the electrical parameters derived from these experiments.

Fig. 4 shows the relative conductivity decay profiles for the studied compositions. While the undoped system, Bi_3YO_6, shows a conductivity decay of around 97% after 900 h, tungsten doping is seen to improve the conductivity stability in all cases. However, this improvement is not linearly correlated to the extent of doping, but reaches a maximum at $x = 0.10$, where the relative conductivity decay after 900 h is only 23%.

For the $x = 0.05$ and 0.10 compositions, diffraction data were collected on powdered samples after 50, 250 and 1000 h annealing in air at 650 °C. Neutron diffraction profiles for these samples are summarised in Fig. 5. It is evident that for both compositions, the pure cubic fluorite structure is maintained up to at least 250 h of annealing. After 1000 h annealing, the $x = 0.05$ composition shows a secondary rhombohedral phase (16.9% weight fraction by multiphase Rietveld analysis). In contrast the $x = 0.10$ composition maintained the pure cubic δ-phase structure for the whole duration of the annealing experiment. The fitted X-ray and neutron diffraction profiles for these samples are given in the supporting information as Figs. S4 to S11, with crystal and refinement parameters summarised in Tables S1 and S2 and refined structural parameters given in Tables S3 and S4. Fig. 6 shows the variation in the refined unit cell parameter for these two compositions over the annealing experiment. Both compositions show similar behaviour with an

initial increase in the lattice dimension up to 250 h, followed by a decrease. The magnitude of these changes is very small with a maximum increase of 0.04% and cannot account for the substantial changes in relative conductivity observed in the annealing experiments. Arrhenius plots showing the ionic and electronic contributions to total conductivity for the $x = 0.10$ composition are shown in Fig. 7. The total conductivity and ionic conductivity plots are coincident, confirming the dominance of ionic transport in this system, with ionic transference numbers in excess of 0.93 at 500 °C and above.

The structure of δ-$Bi_3Y_{1-x}W_xO_{6+3x/2}$ shows oxide ions distributed over three crystallographically distinct sites. O(1) lies on the ideal fluorite 8*c* site (¼, ¼, ¼) in the *Fm*-3*m* space group in the centre of the tetrahedral cavity of the cubic close packed cation lattice. O(2) is a 32*f* site shifted away from the 8*c* site towards the apices of the tetrahedral cavity, allowing the cations to achieve a lower coordination number. O(3) is a 48*i* site and lies outside the tetrahedral cavity. This site is only seen to be occupied in substituted δ-phase bismuth oxides and can be considered to be interstitial to the δ-Bi_2O_3 structure. The oxide ion distribution over these three sites during the annealing experiment is summarised in Fig. 8. There is no significant change in the oxide ion distribution over the duration of the annealing experiment for both compositions. In particular, the oxide ion distribution shows little evidence of any ageing phenomenon [36,37], indicated by a significant change in the relative occupancies of the 8*c* and 32*f* sites.

We have previously shown that thermally induced changes in conductivity behaviour can be correlated to changes in the oxide ion vacancy distribution in other δ-Bi_2O_3 type phases [20,38]. In order to assess possible changes in the local ordering of vacancies a total neutron scattering analysis was performed on a sample of the $x = 0.10$ composition after 1000 h annealing at 650 °C and compared to an analysis of an un-annealed sample of the same composition. The fitted total pair correlation $G(r)$ and structure factors $S(Q)$ profiles are shown in Fig. 9 and reveal almost identical plots. Selected individual pair correlations derived from the RMC models are shown in Fig. 10. Again no obvious differences are seen in the two samples.

Table 2 summarises the bond valence sums, cation coordination numbers and modal and mean M-O contact distances from the RMC analyses for $Bi_3Y_{0.90}W_{0.10}O_{6.15}$ prior to and post annealing for 1000 h at 650 °C. Very little difference is seen in parameters prior to and post annealing. The BVS sums are close to the expected values, confirming the chemical validity of the model. The cation site coordination numbers (integration of all contacts up to 3.3 Å) are close to those expected from the formula i.e. 6.15. The local cation coordination numbers (integrated up to the first minimum in the $g_{ij}(r)$ profiles) show the Bi^{3+} cations to have an average coordination number of around 4.7, consistent with stereochemical activity of the Bi $6s^2$ lone pair, Y^{3+} to have an average coordination number around 5.6 (consistent with a mixture of 5 and 6 coordinate Y^{3+}

cations) and that for W^{6+} around 4.1 (i.e. predominantly tetrahedral). The modal contact distances (the first maximum in the corresponding $g_{ij}(r)$ profile) are generally shorter than the corresponding mean values, but the latter are more directly comparable to values obtained from average crystal structure data. The mean Bi-O, Y-O and W-O values compare well to the corresponding sums of the ionic radii (2.34, 2.28 and 1.80 Å, for 5, 6 and 4 coordination geometries, for Bi^{3+}, Y^{3+} and W^{6+} respectively [39]). The average M-O distances from the RMC models at around 2.28 Å are directly comparable to the weighted average M-O distance from the Rietveld analysis of 2.30 Å both prior to and post annealing.

As seen in other substituted δ-Bi_2O_3 type phases [20,38,40], the number of tetrahedral site vacancies is significantly greater than that predicted assuming oxide ions are located exclusively within the tetrahedral sites (Table 3). As seen in the crystallographic analysis, there is significant occupancy of the 48*i* interstitial site, which results in an increase in the tetrahedral site vacancy concentration. The vacancy pair alignments, <100>, <110> and <111> with respect to the cubic cell have a theoretical ratio of 1:2:1.3. The observed ratios differ significantly, showing a statistical preference for the <100> vacancy pair alignment. This is consistent with proposed models for ionic conductivity in δ-Bi_2O_3 based systems [36,37,41-43]. Additionally, the high number of tetrahedral site vacancies make vacancy clustering necessary and we have previously proposed a cluster model that accommodates 3 vacancies per cell with a vacancy pair ratio close to those observed in the present study [38]. While there is no evidence in the RMC configurations for cation ordering (the metal-metal next nearest neighbour distributions are close to the theoretical values, Table 3), the data indicate a preferred oxide vacancy association with tungsten cations. This is evident in Table 3 as a significant departure from the theoretical values based on a random distribution of vacancies (as was present in the starting model). This is to be expected based on the observed four coordination geometry adopted by W^{6+} in the structure.

3. Conclusions

Tungsten substitution for yttrium in δ-Bi_3YO_6 is seen to improve structural and conductivity stability on prolonged annealing in air at 650 °C, with the least conductivity decay shown in compositions with 10% substitution. Lower or higher levels of substitution offer some enhancement of stability, but extended annealing up to 1000 h eventually yields multiphase systems. In δ-$Bi_3Y_{0.90}W_{0.10}O_{6.15}$, no evidence for significant structural change is observed in either the long-range crystallographic or the short-range scales during prolonged annealing,

The local structure of δ-$Bi_3Y_{0.90}W_{0.10}O_{6.15}$ shows a preference for <100> ordering, in common with other substituted bismuth oxides, reflecting the lowest energy migration pathway, while transference number measurements show the conductivity to be predominantly ionic in nature

at intermediate temperatures. The structure shows a preferred vacancy association with W^{6+} cations suggesting they have role in defect trapping.

While changes in the phase composition in the $Bi_3Y_{1-x}W_xO_{6+3x/2}$ system could account for the observed conductivity decay on prolonged annealing, the fact that no significant structural change other than a tiny increase in lattice parameter is observed in the $x = 0.10$ composition under the same conditions, despite a relative conductivity decay of around 23%, indicates that this is not the only factor. Indeed, the results suggest that the reason for the observed conductivity decay in the $x = 0.10$ composition lies not in the bulk electrolyte itself, but is associated with interfacial phenomena at the electrode/electrolyte interface. If this is the case then it is difficult to quantify to what extent the phase changes in the other compositions contribute to the conductivity decay. Thus if the interfacial issues can be satisfactorily resolved and conductivity decay significantly reduced or eliminated, then the δ-$Bi_3Y_{0.90}W_{0.10}O_{6.15}$ composition appears to represent a truly stable oxide ion conducting electrolyte. We are currently investigating the nature of these interfacial phenomena.

Acknowledgements

We gratefully acknowledge the Science and Technology Facilities Council (STFC), for neutron beam time at ISIS (RB1320124). Dr Ron Smith at ISIS is gratefully acknowledged for his help in neutron data collection. This work was supported by the National Centre, Poland under grant numbers DKO/PL-TW1/6/2013 and UMO-2018/30/M/ST3/00743.

References

1. E.D. Wachsman, K.T. Lee *Science*, 334 (2011) 935.

2. E.D. Wachsman, C.A. Marlowe, K.T. Lee, *Energy Envrion. Sci*. 5 (2012) 5498

3. T. Takahashi, H. Iwahara, Y. Nagaj, *J. Appl. Electrochem*., 2 (1972) 97.

4. G. Mairesse, in Fast Ion Transport in Solids, B. Scrosati, A. Magistris, C.M. Mari, G. Mariotto (Eds.), Kluwer Academic Publishers, Dordrecht, 1993, p271.

5. J.C. Boivin, G. Mairesse, *Chem. Mater*., 10 (1998) 2870.

6. P. Shuk, H.D. Wiemhöfer, U. Guth, W. Göpel, M. Greenblatt, *Solid State Ionics*, 89 (1996) 179.

7. N.M. Sammes, G.A. Tompsett, H. Näfe, F. Aldinger, *J. Eur. Ceram. Soc*., 19 (1999) 1801.

8. A.M. Azad, S. Larose, S.A. Akbar, *J. Mater. Sci*., 29 (1994) 4135.

9. M. Drache, P. Rooussel, J-P. Wignacourt, Chem. Rev. 107 (2007) 80.

10. N. Jiang, E.D. Wachsman, *J. Amer. Ceram. Soc*., 82 (1999) 3057.

11. A. Jaiswal, E.D. Wachsman, *Solid State Ionics*, 177 (2006) 677.

12. M. Camaratta, E Wachsman, *Solid State Ionics*, 178 (2007) 1242.

13. K.Z. Fung H.D. Baek, A. Virkar, *Solid State Ionics*, 52 (1992) 199.

14. D.W. Jung, J.C. Nino, K.L. Duncan, S.R. Bishop, E.D. Wachsman, *Ionics* 16 (2010) 97.

15. A. Watanabe, *Solid State Ionics* 40/41 (1990) 889.

16. A. Watanabe, *Solid State Ionics* 86-88 (1996) 1427.

17. A. Watanabe, M. Sekita, *Solid State Ionics*, 176 (2005) 2429.

18. D. W. Jung, K.L. Duncan E.D. Wachsman, *Acta Materialia*, 58 (2010) 355.

19. I. Abrahams, A. Kozanecka-Szmigiel, F. Krok, W. Wrobel, S.C.M. Chan, J.R. Dygas, *Solid State Ionics* 177 (2006) 1761.

20. I. Abrahams, X. Liu, S. Hull, S.T. Norberg, F. Krok, A. Kozanecka-Szmigiel, M. S. Islam, S.J. Stokes, *Chem. Mater*. 22 (2010) 4435.

21. M. Krynski, W. Wrobel, J. R. Dygas, J. Wrobel, M. Malys, P. Śpiewak, K.J. Kurzydlowski, F. Krok, I. Abrahams, *Solid State Ionics*, 245 (2013) 43.

22. M. Krynski, W. Wrobel, C.E. Mohn, J. R. Dygas, M.Malys, F. Krok1 and I. Abrahams, *Solid State Ionics*, 264 (2014) 49.

23. M. Krynski, W. Wrobel, J. R. Dygas, M.Malys, F. Krok and **I. Abrahams**, *J. Mater. Chem. A*, 3 (2015) 21882.

24. C.D. Ling, R.L. Withers, S.S. Schmid, J.G. Thompson, *J. Solid State Chem.*, 137 (1998) 42.

25. T.E. Crumpton, M.G. Francesconi, G. Greaves, *J. Solid State Chem*., 175 (2003) 197.

26. A. Borowska-Centkowska, F. Krok, I. Abrahams, W. Wrobel, J.R. Dygas, S. Hull, *Solid State Ionics*, 202 (2011) 14.

27. A. Borowska-Centkowska, M. Leszczynska, W. Wrobel, M. Malys, M. Krynski, S. Hull, F. Krok, I. Abrahams, *Solid State Ionics*, 308 (2017) 61.

28. A. C. Larson, R. B. Von Dreele, Los Alamos National Laboratory Report, No. LAUR-86-748, (1987).

29. X.J. Zhang, W.T. Jin, S.J. Hao, Y. Zhao, H. Zhang, *J. Supercond. Nov. Magn*. 23 (2010) 1011.

30. D.A. Keen, *J. Appl. Cryst*., 34 (2001) 172.

31. A. K. Soper, GudrunN and GudrunX: programs for correcting raw neutron and X-ray diffraction data to differential scattering cross section, Report RAL-TR-2011-013, Rutherford Appleton Laboratory Technical, 2011.

32. Tucker, M. G.; Keen, D. A.; Dove, M. T.; Goodwin, A. L.; Hui, Q.; *J. Phys.: Condens. Matter* 19 (2007) 335218.

33. Norberg, S. T.; Tucker, M. G.; Hull, S.; *J. Appl. Crystallogr*. 42 (2009) 179.

34. N.E. Brese, M. O'Keeffe, Acta Crystallogr. B47 (1991) 192.

35. M. Malys, J.R. Dygas, M. Holdynski, A. Borowska-Centkowska, W. Wrobel and M. Marzantowicz, *Solid State Ionics*, 225 (2012) 493.

36. S. Boyapati, E.D. Wachsman, B.C. Chakoumakos, *Solid State Ionics* 138 (2001) 293.

37. S. Boyapati, E.D. Wachsman, N. Jiang, *Solid State Ionics* 140 (2001) 149.

38. M. Leszczynska, X. Liu, W. Wrobel, M. Malys, M. Krynski, S.T. Norberg, S. Hull, F. Krok, I. Abrahams, *Chem. Mater*., 25 (2013) 326.

39. R.D. Shannon, Acta Crystallogr. A32 (1976) 751.

40. A. Borowska-Centkowska, X. Liu, M. Krynski, M. Leszczynska, W. Wrobel, M. Malys, S. Hull, S. T. Norberg, F. Krok and I. Abrahams, RSC Adv. 9 (2019) 9640-9653.

41. A. Walsh, G. W. Watson, D. J. Payne, R. G. Edgell, J. Guo, P. –A. Glans, T. Learmont, K. E. Smith, *Phys. Rev. B.* 2006, **73**, 235104.

42. D. S. Aidhy, J. C. Nino, S. B. Sinnott, E. D. Wachsman, S. R. Phillpot, *J. Am. Ceram. Soc*. 2008, **91**, 2349.

43. M. Yashima, D. Ishimura, *Chem. Phys. Lett*. 2003, **378**, 395.

Table 1. Total conductivities at 300 °C (σ_{300}), 700 °C (σ_{700}) and activation energies in low (ΔE_{LT}) and high (ΔE_{HT}) temperature regions for $Bi_3Y_{1-x}W_xO_{6+3x/2}$ before and after annealing. Estimated standard deviations are given in parentheses.

(a) Low temperature

	before annealing		after annealing	
x	ΔE_{LT} /eV	σ_{300} / S cm^{-1}	ΔE_{LT} /eV	σ_{300} / S cm^{-1}
0.00	1.178(2)	2.95×10^{-5}	1.096(2)	1.98×10^{-6}
0.05	1.161(6)	5.25×10^{-5}	1.018(2)	6.96×10^{-6}
0.10	1.153(9)	4.93×10^{-5}	1.098(4)	4.71×10^{-5}
0.15	1.111(9)	2.87×10^{-5}	1.168(13)	3.82×10^{-6}
0.20	1.129(13)	5.19×10^{-5}	1.122(4)	6.46 10^{-6}

(b) High temperature

	before annealing		after annealing	
x	ΔE_{HT} /eV	σ_{700} / S cm^{-1}	ΔE_{HT} /eV	σ_{700} / S cm^{-1}
0.00	0.729(13)	0.228	0.735(12)	0.123
0.05	0.665(8)	0.307	0.662(14)	0.305
0.10	0.627(11)	0.283	0.631(15)	0.283
0.15	0.670(21)	0.214	0.623(16)	0.196
0.20	0.640(5)	0.245	0.655(9)	0.271

Table 2

Bond valence sums (BVS), M-O coordination numbers (CN) and modal and mean M-O contact distances (Å) from RMC analysis of $Bi_3Y_{0.90}W_{0.10}O_{6.15}$ after annealing in air at 650 °C for 0 and 1000 h. Values are averages of 10 parallel calculations and standard deviations are given in parentheses. M-O distances and local coordination numbers were calculated up to a maximum of 2.79 Å for Bi and Y and 2.24 Å for W (ca. the first minimum in the corresponding $g_{ij}(r)$ profile). Site coordination numbers were derived by integration of $g_{MO}(r)$ to a maximum of 3.30 Å.

		0 h	1000 h
BVS	Bi^{3+}	3.004(3)	2.995(3)
	Y^{3+}	2.994(6)	2.977(5)
	W^{6+}	5.89(2)	5.89(1)
	O^{2-}	1.999(1)	1.992(1)
Site CN	Bi-O	5.95(2)	5.95(1)
	Y-O	6.67(4)	6.68(4)
	W-O	6.01(10)	6.04(9)
Local CN	Bi-O	4.73(3)	4.69(1)
	Y-O	5.59(4)	5.61(2)
	W-O	4.19(7)	4.08(6)
Distances	Bi-O Mode	2.17(3)	2.217(7)
	Bi-O Mean	2.300(1)	2.299(1)
	Y-O Mode	2.08(1)	2.092(7)
	Y-O Mean	2.287(3)	2.288(1)
	W-O Mode	1.70(2)	1.69(3)
	W-O Mean	1.818(5)	1.807(6)
	Av. M-O Mode	2.14(2)	2.175(6)
	Av. M-O Mean	2.285(1)	2.284(1)

Table 3

Defect concentration and distribution parameters derived from RMC analyses of $Bi_3Y_{0.90}W_{0.10}O_{6.15}$ after annealing in air at 650 °C for 0 and 1000 h. Values are averages of 10 parallel calculations and standard deviations are given in parentheses.

	0 h	1000 h	Theoretical
No. tet. vacancies per fluorite cell	3.03(3)	3.16(2)	1.85
100:110:111	1.00:1.72:1.09	1.00:1.74:1.11	1.0:2.0:1.3
$\%vac(NN)_{Bi}$	57.2(3)	57.4(2)	75.0
$\%vac(NN)_{Y}$	24.3(3)	24.2(2)	22.5
$\%vac(NN)_{W}$	18.5(1)	18.5(1)	2.5
$\%Bi(NNN)_{Bi}$	75.5(2)	75.5(2)	75.0
$\%Bi(NNN)_{Y}$	21.9(2)	22.0(2)	22.5
$\%Bi(NNN)_{W}$	2.6(1)	2.6(1)	2.5
$\%Y(NNN)_{Bi}$	72.8(5)	73.0(9)	75.0
$\%Y(NNN)_{Y}$	24.8(6)	24.6(1)	22.5
$\%Y(NNN)_{W}$	2.4(1)	2.5(1)	2.5
$\%W(NNN)_{Bi}$	77.2(1.1)	77.1(1.2)	75.0
$\%W(NNN)_{Y}$	21.7(1.0)	22.1(1.2)	22.5
$\%W(NNN)_{W}$	1.1(5)	0.8(5)	2.5

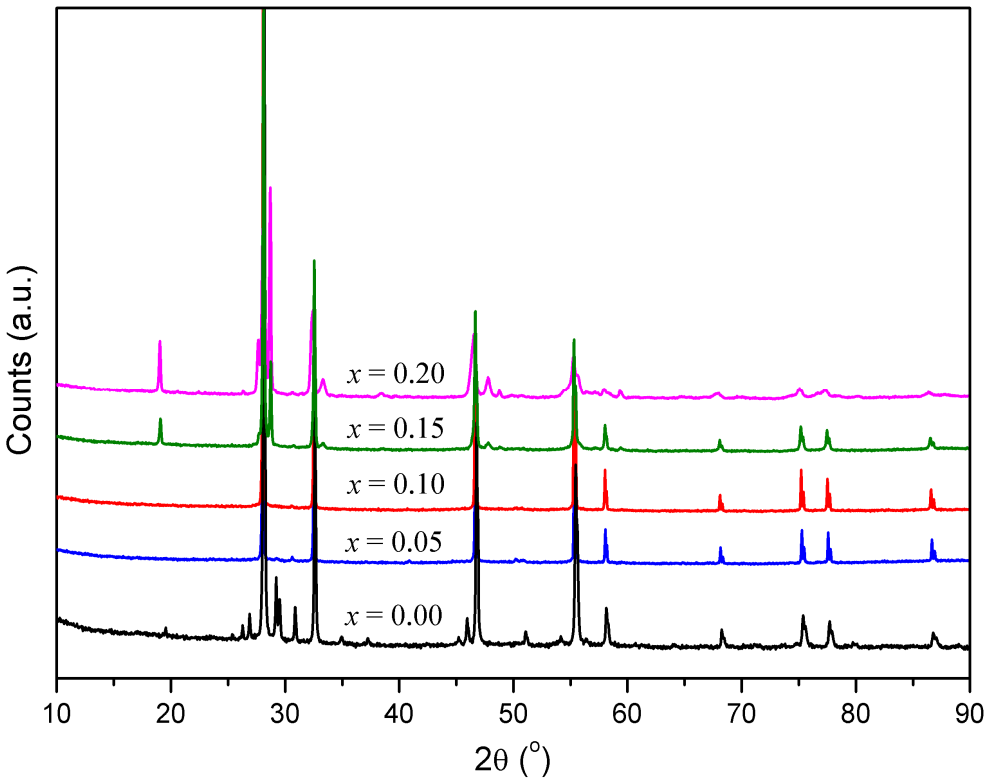

Fig. 1. X-ray diffraction patterns for pellets of composition $Bi_3Y_{1-x}W_xO_{6+3x/2}$ after 200 h annealing in air at 650 °C.

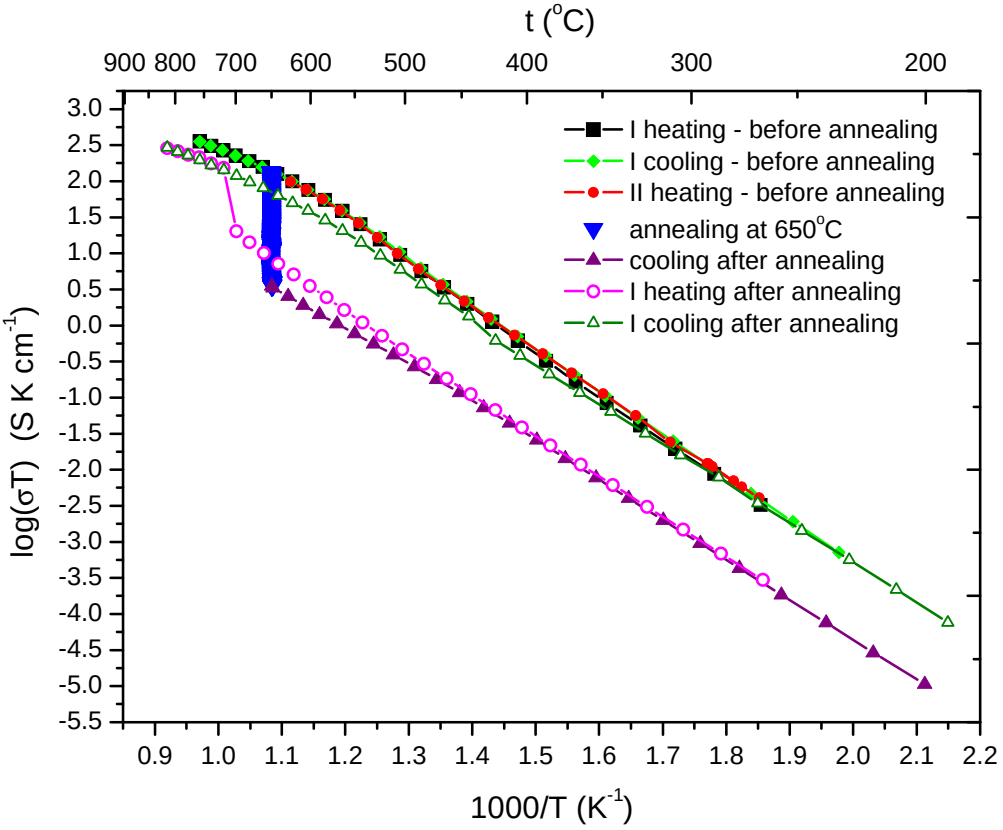

Fig. 2. Arrhenius plot of total conductivity for Bi_3YO_6 –■–/–♦–/–●– - heating up to 850 °C, cooling and heating up to 650 °C before annealing; ▼ - conductivity during annealing at 650 °C for 1100 h; –▲– - cooling after annealing; –O–/–Δ– - heating up to 850 °C and cooling after annealing.

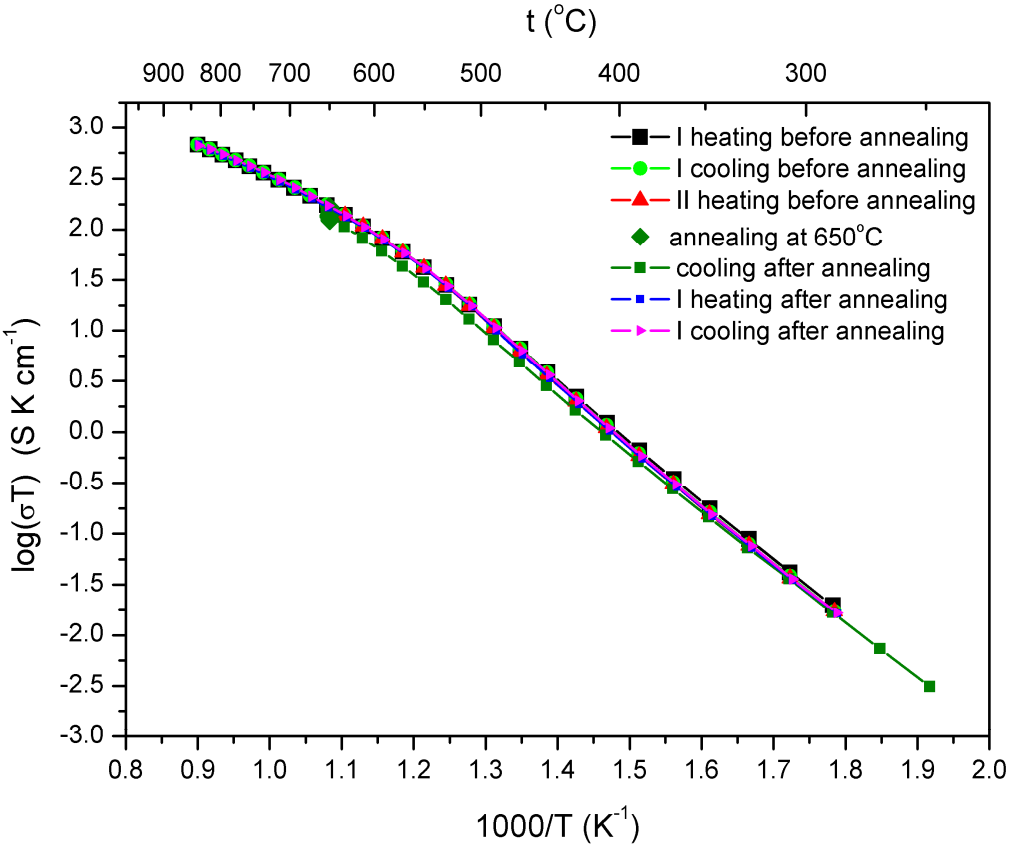

Fig. 3. Arrhenius plot of total conductivity for $Bi_3Y_{0.9}W_{0.1}O_{6.15}$. –●–/–●–/–●– - heating up to 850 °C, cooling and heating up to 650 °C before annealing; ■ - conductivity during annealing at 650 °C for 1100 h; –●– - cooling after annealing; –●–/–●– - heating up to 850 °C and cooling after annealing.

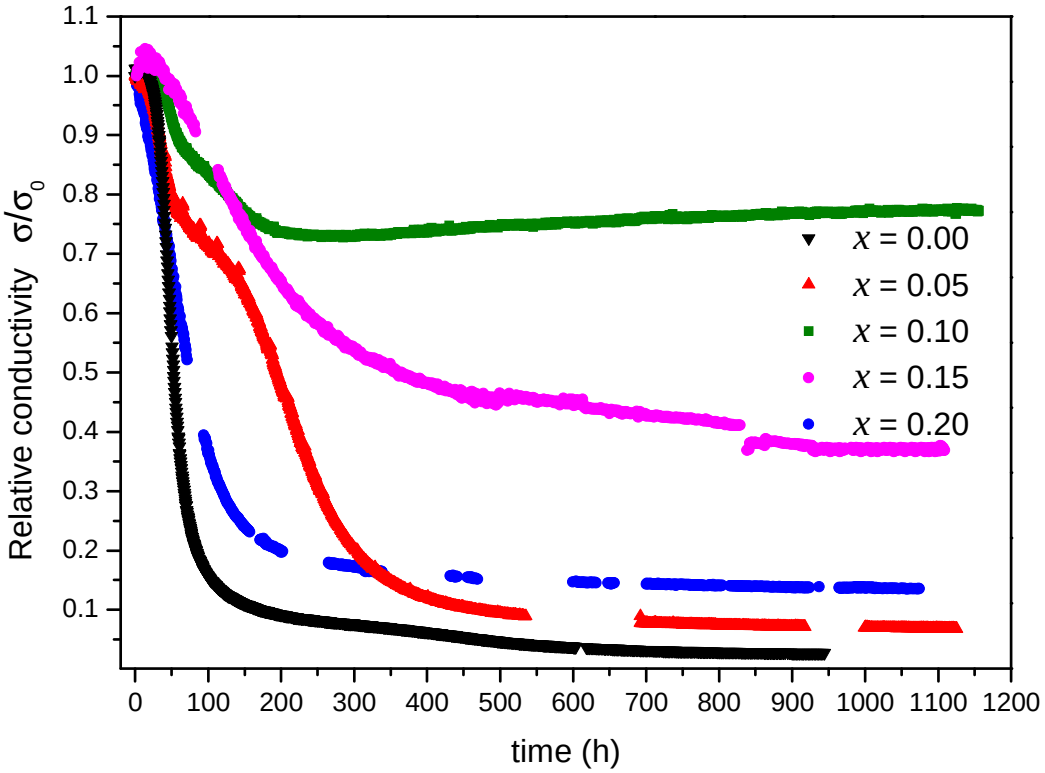

Fig. 4. Variation of relative conductivity with annealing time at 650 °C in air for $Bi_3Y_{1-x}W_xO_{6+3x/2}$ compositions.

(a)

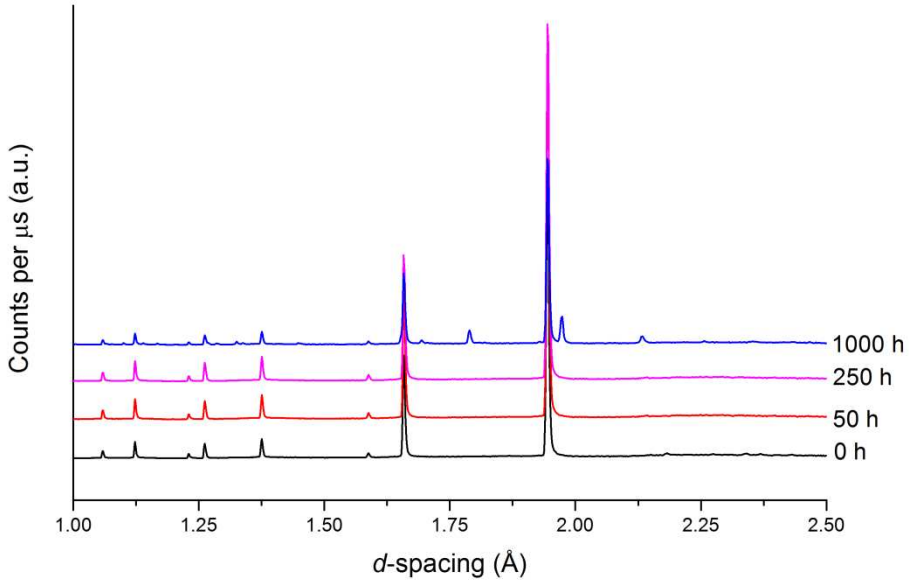

(b)

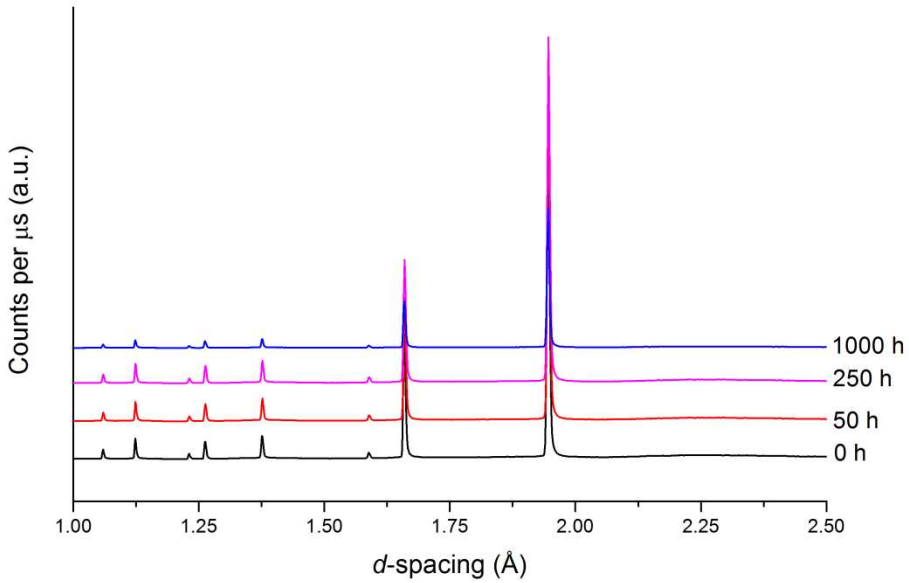

Fig. 5. Detail of neutron diffraction patterns for powder of (a) $Bi_3Y_{0.95}W_{0.05}O_{6.075}$ and (b) $Bi_3Y_{0.90}W_{0.1}O_{6.15}$ for fresh samples and samples after annealing in air at 650 °C for 50 h, 250 h and 1000 h.

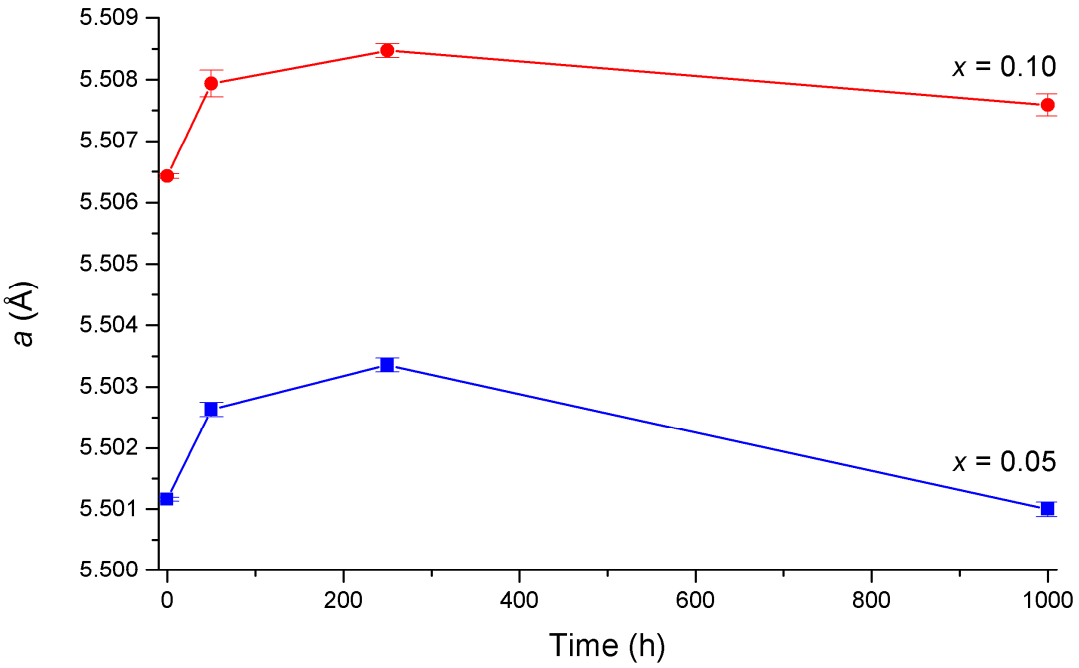

Fig. 6. Variation of cubic lattice parameter in $Bi_3Y_{1-x}W_xO_{6+3x/2}$ with annealing time at 650 °C for x = 0.05 and 0.10 compositions.

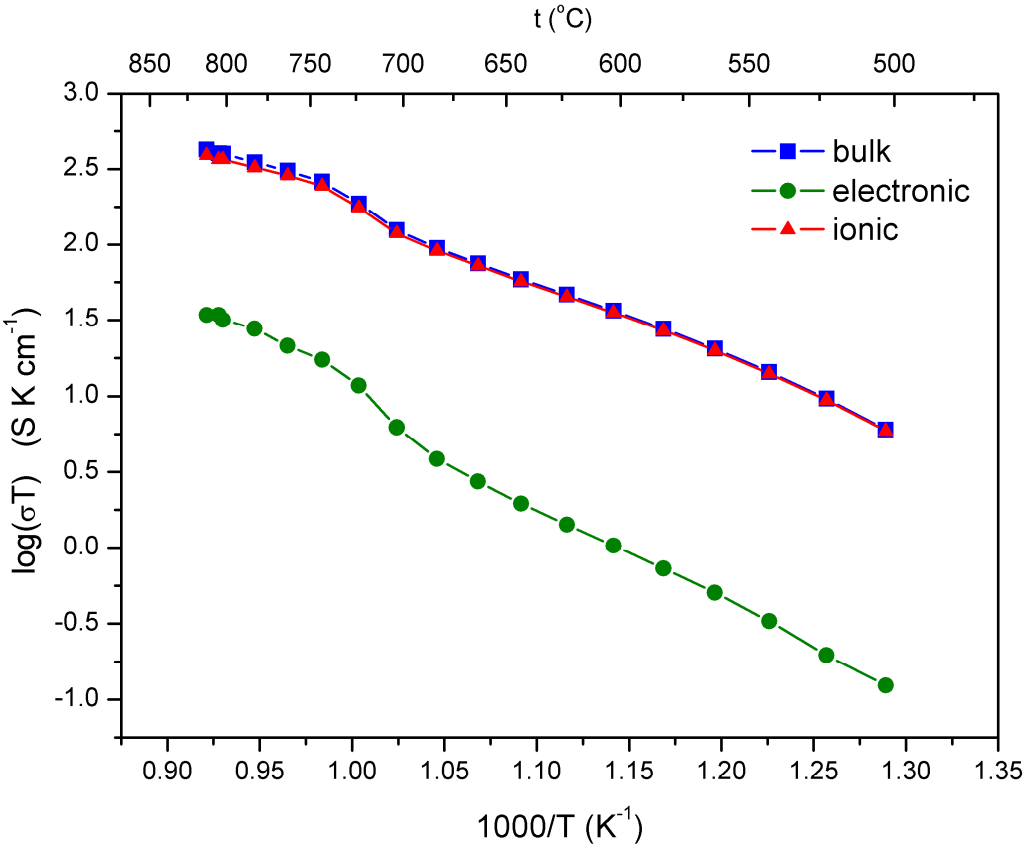

Fig. 7. Thermal variation of bulk, ionic and electronic conductivities for $Bi_3Y_{0.90}W_{0.1}O_{6.15}$

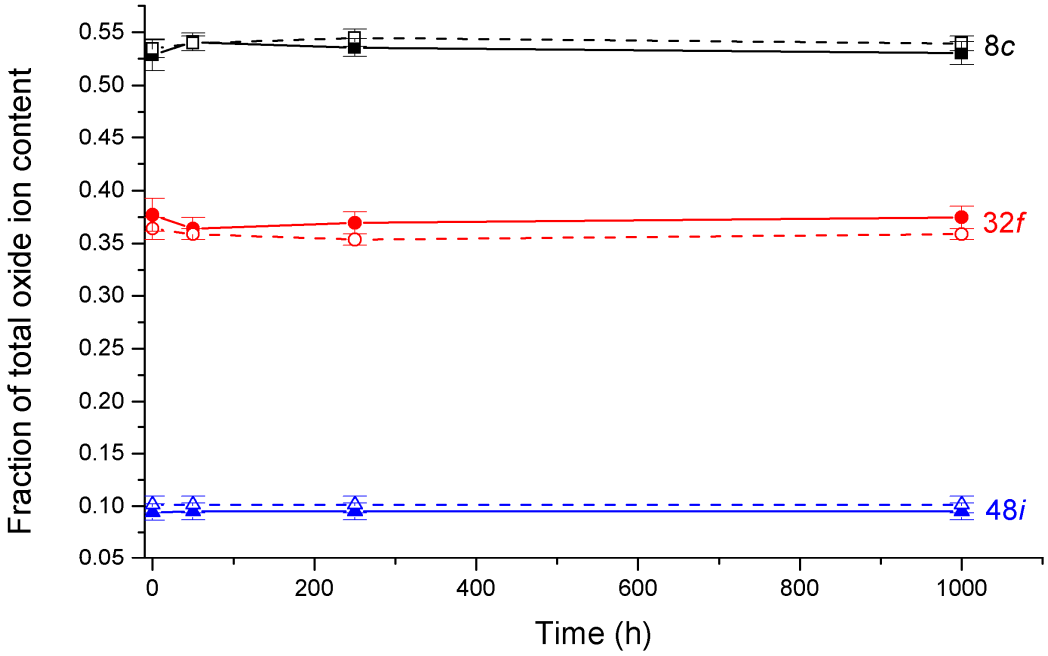

Fig. 8. Variation of oxide ion distribution in $Bi_3Y_{1-x}W_xO_{6+3x/2}$ with annealing time at 650 °C for x = 0.05 (solid line) and 0.10 (dashed line) compositions.

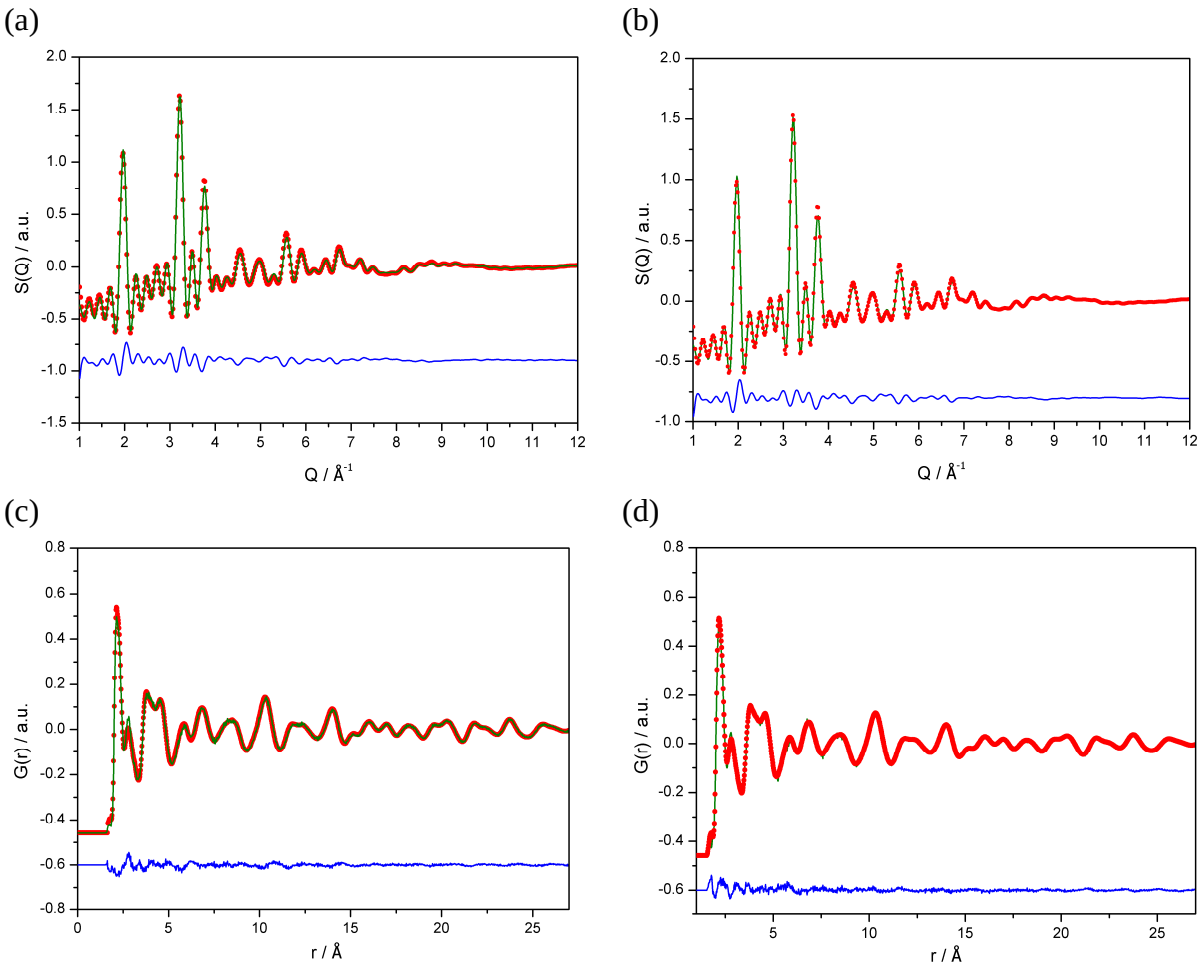

Fig. 9. Fitted (a and b) total scattering S(*Q*) and (c and d) total radial pair distribution functions G(*r*) for $Bi_3Y_{0.90}W_{0.1}O_{6.15}$ on annealing in air at 650 °C for (a and c) 0 h and (b and d) 1000 h.

(a)

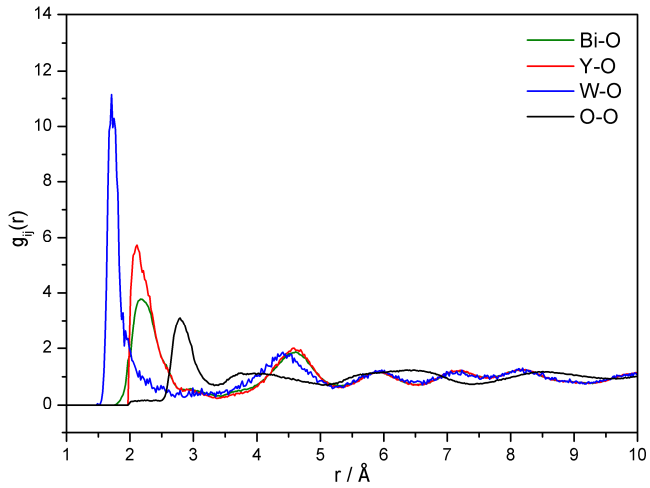

(b)

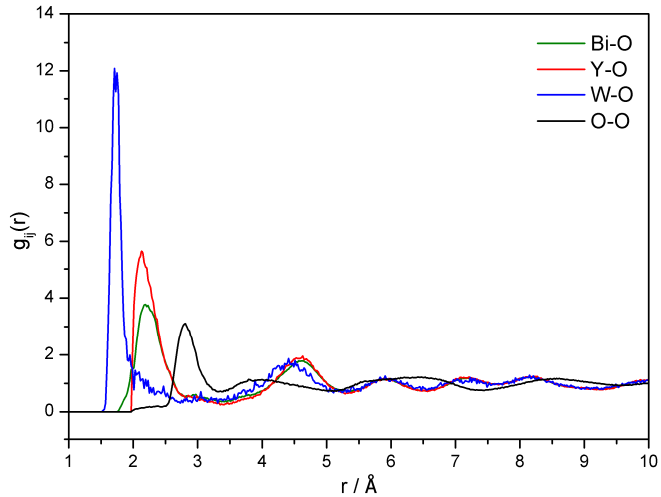

Fig. 10. Selected individual pair correlations from RMC configurations for $Bi_3Y_{0.90}W_{0.1}O_{6.15}$ on annealing in air at 650 °C for (a) 0 h and (b) 1000 h.